IEEE Access
Multidisciplinary ⋮ Rapid Review ⋮ Open Access Journal

Received May 31, 2019, accepted July 6, 2019, date of publication July 9, 2019, date of current version July 29, 2019.

Digital Object Identifier 10.1109/ACCESS.2019.2927617

Internal Voltage Phase-Amplitude Dynamic Analysis With Interface Friendly Back-To-Back Power Converter Average Model for Less Power Electronics-Based More-Electric Ship

KAI NI[1], (Student Member, IEEE), YIHUA HU[1], (Senior Member, IEEE), RUI LIANG[2], (Member, IEEE), HUIQING WEN[3], (Senior Member, IEEE), AND MOHAMMED ALKAHTANI[1]

[1]Department of Electrical Engineering and Electronics, University of Liverpool, Liverpool L69 3GJ, U.K.
[2]School of Electrical and Power Engineering, China University of Mining and Technology, Xuzhou 221116, China
[3]Department of Electrical and Electronic Engineering, Xi'an Jiaotong-Liverpool University, Suzhou 215123, China

Corresponding author: Yihua Hu (y.hu35@liverpool.ac.uk)

This work was supported by the Newton Advanced Fellowship under Grant NAF\R1\191153.

ABSTRACT The advancement in power electronics techniques provides a strong impetus for the adoption of medium-voltage direct current (MVDC) shipboard power system (SPS). However, high fault protection difficulty and cost are the major challenges. In this paper, a partially power decoupled SPS based on the doubly fed induction machine (DFIM) propulsion load is presented to increase the system safety level by using less power electronics. Different from a grid-connected DFIM-based system, the on-board power of the proposed DFIM-SPS is supplied from standalone synchronous generators, and its system dynamics need to be further investigated. An interface friendly average model for the back-to-back power converter (BTBPC) in DFIM-SPS is proposed for system-level dynamic study, which reduces the simulation time and is easy for physical understanding. The stator and BTBPC of DFIM are regarded as separate voltage vectors in the system, and small-signal modeling is carried out in the electromechanical control timescale to analyze the internal voltage phase-amplitude dynamics. The control effects of rotor speed control (RSC), reactive power control (RPC), and phase-locked loop (PLL) are considered in the modeling process. The simulations are performed to study the control effects on DFIM-SPS in MATLAB/Simulink, with the effectiveness of the proposed BTBPC average model validated.

INDEX TERMS Shipboard power system, doubly-fed induction machine, average power converter model, back-to-back power converter, electromechanical control timescale.

NOMENCLATURE

v, i, φ, f, e	Instantaneous values of voltage, current, flux, frequency, internal voltage
V, I, E	Steady-state values of voltage, current and internal voltage
R, L, C	Resistance, inductance, capacitance
X, Z	Reactance, impedance
L_{ls}, L_{lr}	Stator and rotor leakage inductances
L_m	Mutual inductance
L_c, L_s, L_r	Converter-side, stator, and rotor inductances ($L_s = L_m + L_{ls}$; $L_r = L_m + L_{lr}$)
P, Q	Active and reactive powers
$\theta_g, \theta_e, \theta_m, \theta_{slip}, \theta_p$	Grid voltage angle, internal voltage angle, mechanical rotor angle, slip angle, PLL synchronized angle
$\omega_b, \omega_m, \omega_{slip}$	Nominal angular frequency, mechanical rotor angular speed, slip angular speed
δ	Rotor angle deviation
T_{em}, T_m, T_D	Electromagnetic mechanical and damping torques
n_p, H, F	Number of pole pairs, inertia constant, friction factor
X_m, X_l, X_k	Mutual leakage and damping reactance

The associate editor coordinating the review of this manuscript and approving it for publication was Xiaodong Sun.

This work is licensed under a Creative Commons Attribution 4.0 License. For more information, see http://creativecommons.org/licenses/by/4.0/

k_s, k_p, k_i	Stator coupling factor, proportional gain, integral gain
K_a, K_e, K_f	Regulator, exciter, and stabilizer gains
T_a, T_e, T_f	Time constants for regulator, exciter, and stabilizer
S	Switching function
Δ	Small-signal perturbation
pu, div	Per unit, division
Subscripts	
s, r, ss, t	Stator, rotor, source side converter, and total variables
p, i, ω, v, q	PLL, rotor current, rotor speed, voltage, and reactive power related variables
f, k, l	Field winding, damper winding, leakage variables
ub	Unbalanced variable
dc	DC-bus variable
nom	Nominal value
$stab$	Stabilizing value
SG	Variables of synchronous generator
a, b, c	Phases A, B, C
d, q	Direct and quadrature components referred to the synchronous reference frame
0	Variable value at a specific operation point
Superscripts	
$*$	Reference value
p	Variables represented in PLL reference frame

I. INTRODUCTION

The latest more-electric ships (MESs) tend to adopt DC power distribution architectures [1]–[3] due to the benefits of no power factor issue, no skin effect, and easy integration of energy storage systems. The medium-voltage direct-current (MVDC) shipboard power system (SPS) is the representative, where the voltage level ranges from 1kV to 35kV [3]. Power electronic interfaces are extensively used for this type of SPS architecture, which removes the synchronization requirement and bulky low-frequency transformers, and improves the fuel efficiency. However, the SPS stability and reliability are threatened owing to the characteristics of zero inertia [4], [5] and fragile solid-state material [6]. Moreover, high fault protection requirements are presented for DC power distribution, i.e. fast and precise isolation of faulty sections [7], [8], in which case the difficulty and cost of implementing fault protection are high.

The most prominent feature of MVDC-SPS is that the power electronic interfaces have the dominating status in regulating the on-board power flows. For the sake of carrying out system-level studies, average-value modeling (AVM) methods for power converters were presented for MVDC-SPS [9]–[11] to release the computational burden and thus reduce the simulation time. More importantly, dynamic average models can be applied as powerful computational tools for large- and small-signal analysis for power systems [12]. However, the validity of such models depends on the frequency range used. In order to properly investigate the system stability, linearization is one of the commonly applied methods. Generally, there are three categories of AVM methods for linearizing power converter models, including traditional averaging methods [13], [14], generalized-averaging or dynamic phasor methods [15], [16], harmonic domain-based modeling and harmonic state-space modeling [17]–[19]. A comprehensive review and comparison of these linearized modeling methods for AC-DC power converters can be found in [20]. However, these methods are emulated in a mathematical way, which are not straightforward for physical understanding.

The use of AVM methods in SPS has also been widely investigated. The modeling and simulation of low-voltage DC MES by comparing and discussing different AVM methods were carried out in [21]. In [22], a novel AVM approach for MVDC system in the form of differential algebraic equation was presented to derive a more precise approximation of the system dynamic behaviors when comparing with the conventional AVM method. However, as the propulsion module was assumed as a constant power load, the effects of propulsion motor dynamics were neglected. Moreover, the dynamic assessment of source-load interactions in MVDC-SPS was accomplished in [23] by investigating the effects of applying three different source-side converters. Although the effect of source-side converter control strategy was well researched, the impacts caused by the machine-side inverter control were not discussed.

A large number of researchers focused on improving the system safety level by proposing different control strategies for fully rated motor drive systems to improve the stability and reliability of MVDC-SPS [24]–[31]. Although these methods are applicable for certain cases, they do not deal with the intrinsic safety issues caused by applying DC power distribution and extensive use of power electronics. Therefore, from the intrinsic safety point of view, we propose a doubly-fed induction machine (DFIM) propulsion load based SPS to mitigate the dominating status of power electronics for a higher system safety level. A back-to-back power converter (BTBPC) is connected between the rotor and power source, with the stator directly connected to the power source [32]. The system structure of the proposed DFIM-SPS is displayed in Figure 1. It can be seen that the power distribution is not only dependent on power converters, but is also achieved by direct AC power transmission between the stator and power source. In this case, the overall system inertia is increased, and the breakdown of BTBPC does not impede the operation of MES. A partially power decoupled SPS can be obtained, where the tradeoff between AC and DC architectures can be flexibly adjusted to achieve the optimal overall performance.

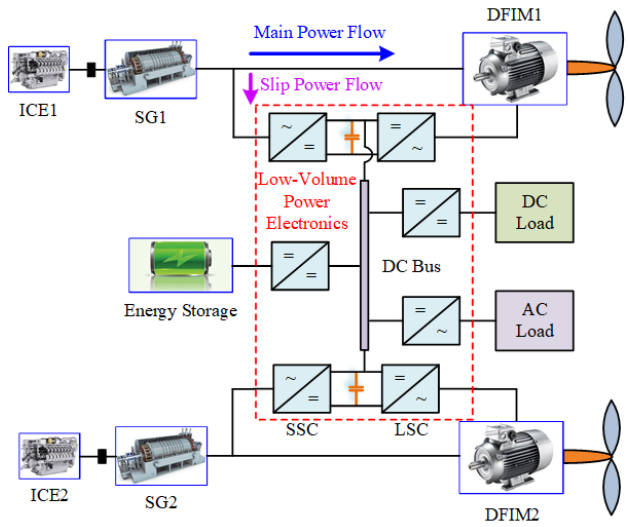

FIGURE 1. The system structure of DFIM-SPS.

In the field of grid-connected DFIM based wind turbines (WTs), the system dynamics were investigated [33]–[37] for the purpose of understanding the physical properties. The DFIM and BTBPC are synthetically represented as a voltage vector in the system, which is difficult to investigate the effects of BTBPC modeling. Moreover, the investigated DFIM-WTs are all connected to power grid. In the case of standalone power systems like SPS, the power source is not an infinite grid, whose system characteristics are to be further studied. In this paper, the modeling of DFIM-SPS is carried out, with an interface friendly average model of BTBPC presented for system-level study. A small-signal model is established to analyze the internal voltage phase-amplitude dynamics, with the control effects of rotor speed control (RSC), reactive power control (RPC) and phase-locked loop (PLL) taken into account.

The existing studies on DFIM small-signal modeling are all based on grid-connected WTs, which have different system dynamic behaviors from the proposed DFIM-SPS. In addition, the effects of BTBPC system-level average model on the system performance have not been taken into account in these studies. Moreover, compared with the existing AVM strategies for power electronic converters, the proposed BTBPC average model is interface friendly and easy to be physically understood. The internal voltage phase-amplitude dynamic analysis in a DFIM-SPS is carried out for the first time in electromechanical control timescale, which is the main contribution of this paper.

The paper structure is organized as follows: Section II describes the proposed DFIM-SPS. In Section III, the models of the main power components in DFIM-SPS are illustrated. Then, the small-signal model for investigating the stator phase-amplitude dynamics is presented by linearization and transfer function deductions in Section IV. In Section V, simulation studies are carried out to validate the proposed BTBPC average model, and investigate the effects of RSC, RPC and PLL controller parameters on the BTBPC average model based DFIM-SPS. Finally, the conclusion is given in Section VI.

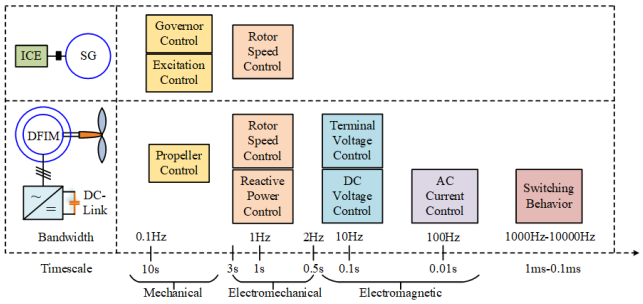

FIGURE 2. Multi-timescale characteristics of DFIM-SPS.

II. SYSTEM DESCRIPTION

DFIM-SPS is a complicated isolated grid that consists of multiple timescales for the onboard power components. The synchronous generator (SG) and DFIM are regarded as the source and load of DFIM-SPS, respectively, and they need to be properly controlled to maintain the power balance of the system, thus ensuring the stable system operation. Different control timescales are presented in this system, whose details are displayed in Figure 2.

As can be seen from Figure 2, there are two main components to be controlled, which are the SG driven by an internal combustion engine (ICE), and the DFIM loaded by a propeller. The system-level analysis can be carried out mainly in three timescales, which are the mechanical, electromechanical and electromagnetic control timescales. However, the high switching speed for power converters greatly prolongs the simulation time if the detailed power converter model is applied. Therefore, with the purpose of conducting system-level studies, where the details of switching behaviors are not required, the average model of BTBPC is to be used in DFIM-SPS to shorten the simulation time. For the power source, the governor and excitation controls are typically in mechanical control timescale, which represents a large time constant of tens of seconds. In terms of the load, the propeller control is accomplished in the mechanical control timescale. These modules respond slowly, and they can be assumed to operate in steady states when referring to the electromechanical control timescale. On the other hand, the DC-bus voltage is to be kept at a constant value by using the source-side converter (SSC), whose response time constant is around 0.1s. Moreover, the current control loop responds faster, which has a bandwidth of around 100Hz. These responses are too fast, so that they cannot be efficiently applied to study the interactions between the power source and load. In this paper, the RSC and RPC that are in the electromechanical control timescale are the main focus, and they play the most important role in assessing the system dynamics of DFIM-SPS with respect to the source-load interactions. Since around 80% of the on-board power is supplied to propulsion loads [38], the service loads are not taken

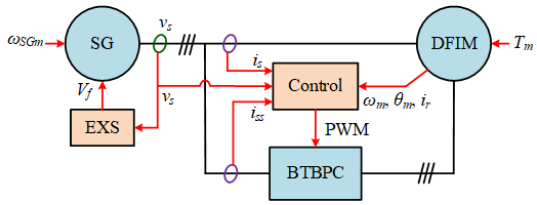

FIGURE 3. The main power components in DFIM-SPS and their control.

into consideration. The effects of cables are also neglected as the distance between the power source and load is much shorter than that of an onshore grid. Therefore, only the effects of SG, BTBPC, and DFIM on system performance are taken into consideration in the presented work.

When studying the system dynamic performance in the electromechanical control timescale, the dynamics in the other control timescales are neglected, and the following assumptions are made: 1) The reference values of rotor speed and reactive power are constant. 2) The DC-bus voltage can track its reference all the time. 3) The SSC-side currents can track their references instantly. 4) The transient dynamics of stator flux, rotor flux, and inductor currents are neglected.

III. DFIM-SPS MODELLING

The basic unit of power components for a DFIM-SPS is displayed in Figure 3, where the SG, BTBPC and DFIM are presented as the power source, conversion stage, and load, respectively. The SG is controlled by applying an excitation system (EXS), while the control of DFIM is based on that of the load-side converter (LSC) in BTBPC. The variables of SG are with the subscript "*SG*", while no additional subscript is added for the variables of DFIM.

A. SG AND EXS

In this paper, a salient-pole SG and a type DC1A EXS [39] are applied. The rotor parameters are seen from the stator sides. There can be a number of damping windings for the equivalent circuit in the rotor reference frame, but only one damping winding is presented for either the d or q equivalent circuit for simplicity. In the dq reference frame, the field winding only exists in the d axis. The electrical model of SG in the dq frame is displayed in Figure 4.

The vectors of voltage, current and flux for SG are defined as below.

$$\mathbf{v_{SG}} = [v_{SGq} \quad v_{SGd} \quad v_{SGfd} \quad v_{SGkd} \quad v_{SGkq}]^{\mathrm{T}} \tag{1}$$

$$\mathbf{i_{SG}} = [i_{SGq} \quad i_{SGd} \quad i_{SGfd} \quad i_{SGkd} \quad i_{SGkq}]^{\mathrm{T}} \tag{2}$$

$$\boldsymbol{\varphi}_{\mathbf{SG}} = [\varphi_{SGq} \quad \varphi_{SGd} \quad \varphi_{SGfd} \quad \varphi_{SGkd} \quad \varphi_{SGkq}]^{\mathrm{T}} \tag{3}$$

Therefore, the voltage and flux equations of SG are

$$\mathbf{v_{SG}} = \mathbf{R_{SG}}\mathbf{i_{SG}} + \frac{d\boldsymbol{\varphi}_{\mathbf{SG}}}{dt} + \boldsymbol{\omega}_{\mathbf{SG}}\boldsymbol{\varphi}_{\mathbf{SG}} \tag{4}$$

$$\boldsymbol{\varphi}_{\mathbf{SG}} = \mathbf{L_{SG}}\mathbf{i_{SG}} \tag{5}$$

where

$$\mathbf{R_{SG}} = \mathrm{diag}(R_{SGs}, R_{SGs}, R_{SGfd}, R_{SGkd}, R_{SGkq}) \tag{6}$$

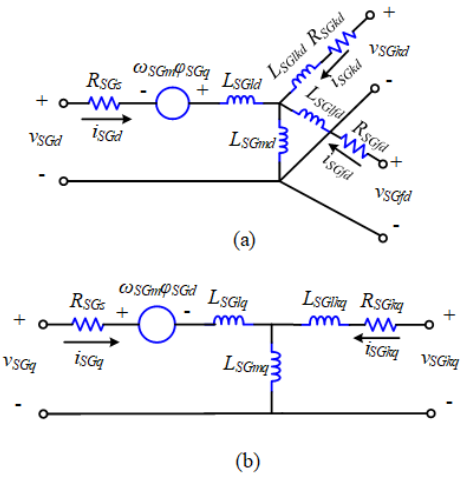

FIGURE 4. SG electrical model in dq frame (a) d-axis (b) q-axis.

$$\boldsymbol{\omega}_{\mathbf{SG}} = \begin{bmatrix} 0 & \omega_{SGm} & 0 & 0 & 0 \\ -\omega_{SGm} & 0 & 0 & 0 & 0 \\ 0 & 0 & 0 & 0 & 0 \\ 0 & 0 & 0 & 0 & 0 \\ 0 & 0 & 0 & 0 & 0 \end{bmatrix} \tag{7}$$

$$\mathbf{L_{SG}} = \begin{bmatrix} L_{SGq} & 0 & 0 & 0 & L_{SGmq} \\ 0 & L_{SGd} & L_{SGmd} & L_{SGmd} & 0 \\ 0 & L_{SGmd} & L_{SGfd} & L_{SGmd} & 0 \\ 0 & L_{SGmd} & L_{SGmd} & L_{SGkd} & 0 \\ L_{SGmq} & 0 & 0 & 0 & L_{SGkq} \end{bmatrix} \tag{8}$$

The mechanical model is represented by the following two equations.

$$\frac{d\omega_{SGm}}{dt} = \frac{1}{2H_{SG}}(T_{SGm} - T_{SGem} - T_{SGD}) \tag{9}$$

$$\frac{d\delta}{dt} = \omega_{SGm} - \omega_b \tag{10}$$

According to the swing equation (9), the change in rotor speed depends on the values of rotor inertia, electromagnetic, mechanical and damping torques. While the change in the deviation angle is determined by the deference between the actual rotor speed and base angular frequency.

The SG stator voltage $\mathbf{v_{SG}}$ is regulated by a type DC1A EXS to provide the field voltage $V_f(v_{SGfd})$. After the active voltage regulation (AVR) process, an exciter is applied to generate the field voltage. Moreover, a stabilizer is added to feed the field voltage component back. The control block diagram for EXS is shown in Figure 5.

The terminal voltage V_T, which is the magnitude of $\mathbf{v_{SG}}$ by excluding the high-order harmonic components, is also applied as a feedback, since it is produced by the magnetic flux induced by the field voltage. The input voltage of EXS is defined as

$$V_{in} = V^* + \frac{V_{f0}}{K_a} + V_{stab} - V_T \tag{11}$$

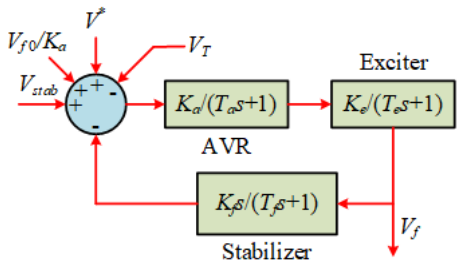

FIGURE 5. Control block diagram of DC1A EXS for SG.

Therefore, the field voltage can be expressed by

$$V_f = \frac{K_aK_e(T_fs+1)}{(T_as+1)(T_es+1)(T_fs+1)+K_aK_eK_fs}V_{in} \quad (12)$$

B. DFIM

By orienting the d-axis in the same direction as that of the stator voltage vector, the voltage and flux equations for DFIM dq model in the synchronous reference frame are derived in the same forms as (4) and (5), respectively. While the expressions for $\mathbf{v}$, $\mathbf{i}$, $\boldsymbol{\varphi}$, $\mathbf{R}$, $\boldsymbol{\omega}$ and $\mathbf{L}$ are different,

$$\mathbf{v} = [v_{sd}\ \ v_{sq}\ \ v_{rd}\ \ v_{rq}\ ]^{\mathrm{T}} \quad (13)$$

$$\mathbf{i} = [i_{sd}\ \ i_{sq}\ \ i_{rd}\ \ i_{rq}\ ]^{\mathrm{T}} \quad (14)$$

$$\boldsymbol{\varphi} = [\varphi_{sd}\ \ \varphi_{sq}\ \ \varphi_{rd}\ \ \varphi_{rq}\ ]^{\mathrm{T}} \quad (15)$$

$$\mathbf{R} = \mathrm{diag}(R_s, R_s, R_r, R_r) \quad (16)$$

$$\boldsymbol{\omega} = \begin{bmatrix} 0 & -\omega_b & 0 & 0 \\ \omega_b & 0 & 0 & 0 \\ 0 & 0 & 0 & -\omega_{slip} \\ 0 & 0 & \omega_{slip} & 0 \end{bmatrix} \quad (17)$$

$$\mathbf{L} = \begin{bmatrix} L_s & 0 & L_m & 0 \\ 0 & L_s & 0 & L_m \\ L_m & 0 & L_r & 0 \\ 0 & L_m & 0 & L_r \end{bmatrix} \quad (18)$$

The electromagnetic torque and the kinetic equation of DFIM are expressed as

$$T_{em} = 1.5n_pL_m(i_{rd}i_{sq} - i_{rq}i_{sd}) \quad (19)$$

$$\frac{d\omega_m}{dt} = \frac{1}{2H}(T_{em} - T_m - T_D) \quad (20)$$

The electromagnetic torque T_{em} is produced by the mutual interactions of stator and rotor dq currents, and the same principle of (9) is applied to the kinetic equation (20).

C. DETAILED MODEL OF BTBPC

There are two power converters in the BTBPC, which are the SSC and LSC. The SSC is directly connected to the AC power transmission line, while the LSC is connected to the rotor of DFIM. The topology of BTBPC is displayed in Figure 6.

The DC-link capacitor C_{dc} is installed to decouple the power regulation of SSC and LSC. The positive direction of power flow is from the SSC to LSC. S_{ssa}, S_{ssb} and S_{ssc} are defined as the switching functions of power switches in the three phases of SSC, while S_{la}, S_{lb} and S_{lc} are defined as the

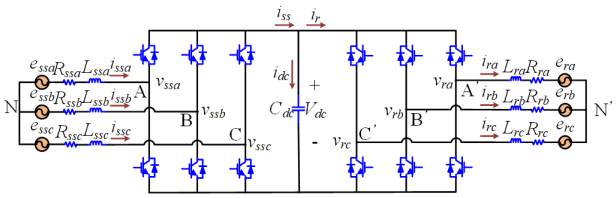

FIGURE 6. BTBPC topology.

switching functions of those of LSC. Therefore, the three-phase model of BTBPC can be expressed as

$$\begin{cases} L_{ssx}\dfrac{di_{ssx}}{dt} = e_{ssx} - R_{ssx}i_{ssx} - \dfrac{e_{ssa}+e_{ssb}+e_{ssc}}{3} \\ -[S_{ssx} - \dfrac{S_{ssa}+S_{ssb}+S_{ssc}}{3}]V_{dc}, \\ \qquad x = a, b, c \\ L_{rx}\dfrac{di_{rx}}{dt} = -e_{rx} - R_{rx}i_{rx} + \dfrac{e_{ra}+e_{rb}+e_{rc}}{3} \\ +[S_{lx} - \dfrac{S_{la}+S_{lb}+S_{lc}}{3}]V_{dc}, \\ \qquad x = a, b, c \\ C_{dc}\dfrac{V_{dc}}{dt} = (S_{ssa}i_{ssa} + S_{ssb}i_{ssb} + S_{ssc}i_{ssc}) - i_r \\ = i_{ss} - (S_{la}i_{ra} + S_{lb}i_{rb} + S_{lc}i_{rc}) \end{cases} \quad (21)$$

$$\begin{cases} v_{ssx} = [S_{ssx} - \dfrac{S_{ssa}+S_{ssb}+S_{ssc}}{3}]V_{dc}, & x = a, b, c \\ v_{rx} = [S_{lx} - \dfrac{S_{la}+S_{lb}+S_{lc}}{3}]V_{dc}, & x = a, b, c \\ i_{ss} = S_{ssa}i_{ssa} + S_{ssb}i_{ssb} + S_{ssc}i_{ssc} \\ i_r = S_{la}i_{ra} + S_{lb}i_{rb} + S_{lc}i_{rc} \end{cases} \quad (22)$$

Substituting (22) into (21), the three-phase model can be updated as

$$\begin{cases} L_{ssx}\dfrac{di_{ssx}}{dt} = e_{ssx} - R_{ssx}i_{ssx} - \dfrac{e_{ssa}+e_{ssb}+e_{ssc}}{3} - v_{ssx}, \\ \qquad x = a, b, c \\ L_{rx}\dfrac{di_{rx}}{dt} = -e_{rx} - R_{rx}i_{rx} + \dfrac{e_{ra}+e_{rb}+e_{rc}}{3} + v_{rx}, \\ \qquad x = a, b, c \\ C_{dc}\dfrac{V_{dc}}{dt} = i_{ss} - i_r \end{cases} \quad (23)$$

Assume that the three phases at both the source and load sides are balanced ($R_{ssa} = R_{ssb} = R_{ssc} = R_{ss}$; $L_{ssa} = L_{ssb} = L_{ssc} = L_{ss}$; $R_{ra} = R_{rb} = R_{rc} = R_r$; $L_{ra} = L_{rb} = L_{rc} = L_r$). The BTBPC dq model is derived as

$$\begin{cases} L_{ss}\dfrac{d\mathbf{i_{ssdq}}}{dt} = \mathbf{e_{ssdq}} - R_{ss}\mathbf{i_{ssdq}} - \mathbf{v_{ssdq}} - \mathrm{j}\omega_eL_{ss}\mathbf{i_{ssdq}} \\ L_r\dfrac{d\mathbf{i_{rdq}}}{dt} = -\mathbf{e_{rdq}} - R_r\mathbf{i_{rdq}} + \mathbf{v_{rdq}} + \mathrm{j}\omega_{slip}L_r\mathbf{i_{rdq}} \\ C_{dc}\frac{V_{dc}}{dt} = i_{ss} - i_r \end{cases} \quad (24)$$

D. INTERFACE FRIENDLY AVERAGE MODEL OF BTBPC

In the detailed BTBPC model, the switching functions are obtained by comparing the instantaneous values of carrier

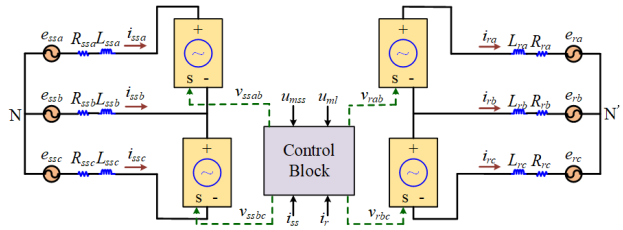

FIGURE 7. Equivalent circuit of proposed BTBPC average model.

wave u_c and modulated wave u_m.

$$S = \begin{cases} 1, & u_m > u_c \\ 0, & u_m \le u_c \end{cases} \tag{25}$$

Since the switching frequency of AC-DC power converter is at the level of several thousands to tens of thousands of Hz, the step time used in the simulation needs to be small enough to construct the valid carrier wave.

When it comes to the system-level analysis, the details of switching functions are not concerned. In this paper, only the system dynamics in the electromechanical control timescale are taken into account. Instead of using the detailed BTBPC model that illustrates the switching details, an interface friendly average model is applied to represent the BTBPC as four controlled voltage sources, which are placed between phases A and B, and between phases B and C at the SSC and LSC sides, respectively. The three-phase modulated signals and current values are the inputs for the control block to obtain the phase-to-phase voltages. The equivalent circuit for BTBPC average model is displayed in Figure 7, and the phase-to-phase voltages for the four controlled voltage sources are calculated by

$$\begin{cases} v_{ssab} = 0.5V_{dc}(u_{mssa} - u_{mssb}) \\ v_{ssbc} = 0.5V_{dc}(u_{mssb} - u_{mssc}) \\ v_{rab} = 0.5V_{dc}(u_{mla} - u_{mlb}) \\ v_{rbc} = 0.5V_{dc}(u_{mlb} - u_{mlc}) \end{cases} \tag{26}$$

In addition, the magnitude for any of these voltage values should be smaller than V_{dc}. The value of V_{dc} can be derived according to the following equation.

$$V_{dc} = \frac{1}{C_{dc}} \int \frac{P_{ss} - P_r}{V_{dc}} dt \tag{27}$$

where

$$P_{ss} = v_{ssab} i_{ssa} - v_{ssbc} i_{ssc} \tag{28}$$

$$P_r = v_{rab} i_{ra} - v_{rbc} i_{rc} \tag{29}$$

IV. SMALL-SIGNAL MODELLING OF DFIM INTERNAL VOLTAGE PHASE-AMPLITUDE DYNAMICS

A DFIM is deemed as a two-port electric machine that regulates power by two paths, where the AC power path is directly connected to its stator, and the power electronic path is connected to its rotor through BTBPC. Therefore, the stator, rotor, SSC and LSC can all be regarded as voltage vectors

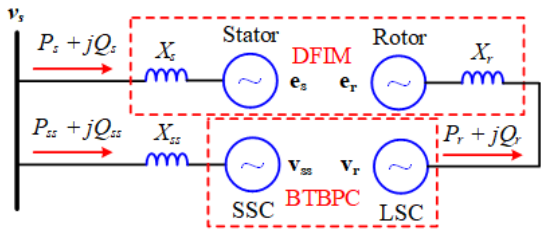

FIGURE 8. Equivalent circuits of DFIM and BTBPC represented by voltage vectors.

to show their external characteristics in the DFIM-SPS. The resistances in the circuit are neglected as they are small compared to the corresponding reactance counterparts. The equivalent DFIM and BTBC circuits represented by voltage vectors are displayed in Figure 8. As defined in [35], $\mathbf{e_s}$ is the internal voltage of DFIM, which is expressed as

$$\mathbf{e_{sdq}} = \mathrm{j}X_m \mathbf{i_{rdq}} \tag{30}$$

A. LINEARIZATION OF INTERNAL VOLTAGE VECTOR

As the stator of DFIM is directly connected to the power source, and the main power flow is injected into the propulsion system through the stator, it is of paramount importance to investigate the phase-amplitude dynamics of $\mathbf{e_s}$.

The dq components of $\mathbf{e_s}$ are expressed as

$$\begin{cases} e_{sd}^p = e_s \cos\theta_e^p = -X_m i_{rq}^p \\ e_{sq}^p = e_s \sin\theta_e^p = X_m i_{rd}^p \end{cases} \tag{31}$$

The superscript "p" indicates that the dq components project into the dq reference frame defined by PLL. Take the partial derivative of θ_e^p at some operation point and combine the two equations, $\Delta\theta_e^p$ can be derived as

$$\Delta\theta_s^p = \frac{X_m \Delta i_{rq}^p \sin\theta_{e0}^p + X_m \Delta i_{rd}^p \cos\theta_{e0}^p}{E_{s0}} \tag{32}$$

At a specific operation point, the amplitude of $\mathbf{e_s}$ is expressed as E_{s0}, as shown in (32). In the steady state, $\theta_{e0}^p = -\pi/2$, so $\sin\theta_{e0}^p = -1$ and $\cos\theta_{e0}^p = 0$, and (32) is updated as

$$\Delta\theta_e^p = -\frac{X_m \Delta i_{rq}^p}{E_{s0}} \tag{33}$$

By applying the similar process, Δe_s can be obtained as

$$\Delta e_s = -X_m \Delta i_{rq}^p \cos\theta_{e0}^p + X_m \Delta i_{rd}^p \sin\theta_{e0}^p \tag{34}$$

By applying $\sin\theta_{e0}^p = -1$ and $\cos\theta_{e0}^p = 0$, (34) is updated as

$$\Delta e_s = -X_m \Delta i_{rd}^p \tag{35}$$

B. LINEARIZATION OF RSC AND RPC

As this paper focuses on the system dynamics of DFIM-SPS in electromechanical control timescale, the DC-bus voltage V_{dc} is assumed to be stable, thus only the control of LSC is considered. The d and q axis rotor currents are controlled respectively for controlling the electromagnetic torque T_{em}

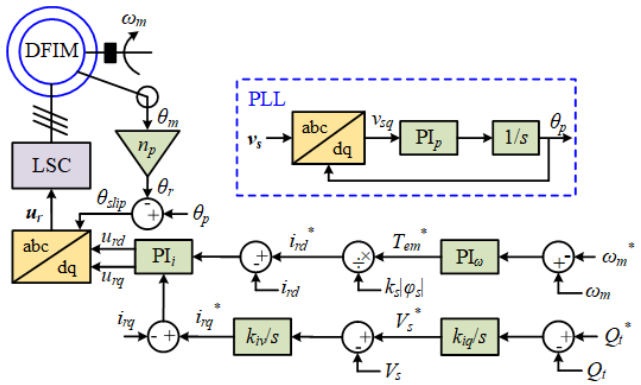

FIGURE 9. Control block diagram including RPC and RSC for DFIM.

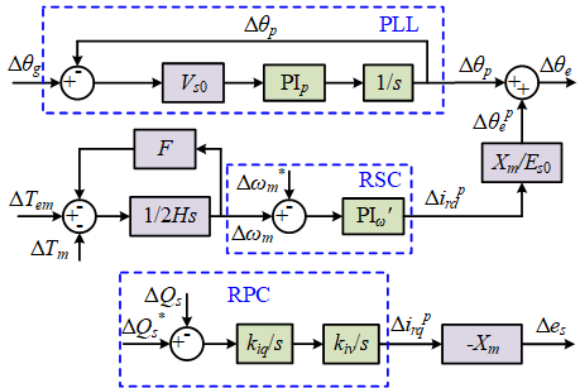

FIGURE 10. Block diagram of small-signal model of DFIM internal voltage phase-amplitude dynamics.

and the terminal voltage v_s, whose reference values are derived from RSC and RPC, respectively, which are

$$i_{rd}^* = \frac{(\omega_m - \omega_m^*)(k_{p\omega} + k_{i\omega}/s)}{k_s\varphi_s} \tag{36}$$

$$i_{rq}^* = [(Q_t^* - Q_t)k_{iq}/s - v_s]k_{iv}/s \tag{37}$$

where $k_s = L_m/L_s$ is the stator coupling factor. The reference value of d-axis rotor current i_{rd}^* is determined by RSC, while that of q-axis rotor current i_{rq}^* is decided by RPC. The control block diagram including RSC and RPC is displayed in Figure 9.

The RSC and RPC are linearized to describe the small-signal values of dq rotor currents.

$$\Delta i_{rd}^p = (\Delta\omega_m - \Delta\omega_m^*)(k'_{p\omega} + k'_{i\omega}/s) \tag{38}$$

$$\Delta i_{rq}^p = (\Delta Q_t^* - \Delta Q_t)k_{iq}k_{iv}/s^2 \tag{39}$$

where $k'_{p\omega} = (k_{p\omega}/k_s\varphi_{s0})$ and $k'_{i\omega} = (k_{i\omega}/k_s\varphi_{s0})$.

C. LINEARIZATION OF PLL

The output angle of PLL θ_p is obtained by implementing PI control and another integration for the q-axis component of $\mathbf{v_s}$.

$$\theta_p = v_{sq}(k_{pp} + k_{ip}/s)/s = v_s \sin\theta_g^p(k_{pp} + k_{ip}/s)/s \tag{40}$$

Linearizing it at some operation point,

$$\Delta\theta_p = V_{s0}\cos\theta_{g0}^p\Delta\theta_g^p(k_{pp}/s + k_{ip}/s^2) \tag{41}$$

Under the steady state, the difference between grid voltage angle θ_g and synchronized angle of PLL θ_p is 0, thus (41) can be modified as

$$\Delta\theta_p = V_{s0}\Delta\theta_g^p(k_{pp}/s + k_{ip}/s^2) \tag{42}$$

The internal voltage phase and amplitude dynamics can be obtained based on (33)-(35) and (38)-(42) by taking PLL, RSC and RPC into account. As the small-signal model is established in the electromechanical control timescale, the SSC dq currents i_{ssd} and i_{ssq} track their reference values, so does the terminal voltage v_s. Therefore, the small-signal model of DFIM internal voltage phase-amplitude dynamics is illustrated in Figure 10.

D. TRANSFER FUNCTIONS FOR $\Delta\theta_e$ AND Δe_s

The final step in small-signal modeling for internal voltage phase-amplitude dynamics study is to derive the transfer functions for $\Delta\theta_e$ and Δe_s. Therefore, the grid voltage angle $\Delta\theta_g$ needs to be eliminated.

The expressions of the active and reactive powers delivered to the stator of DFIM are shown below.

$$P_s = \frac{e_s v_s \sin(\theta_g - \theta_e)}{X_s} \tag{43}$$

$$Q_s = \frac{e_s^2 - e_s v_s \cos(\theta_g - \theta_e)}{X_s} \tag{44}$$

Linearizing the above two equations, and since $\theta_g = \theta_p$ at a specific operation point, the following equations are derived.

$$\begin{aligned} X_s\Delta P_s = &-V_{s0}\Delta e_s \sin\theta_{e0}{}^p - E_{s0}\Delta v_s \sin\theta_{e0}{}^p \\ &+ E_{s0}V_{s0}\Delta\theta_g \cos\theta_{e0}{}^p - E_{s0}V_{s0}\Delta\theta_e \cos\theta_{e0}{}^p \end{aligned} \tag{45}$$

$$\begin{aligned} X_s\Delta Q_s = &\ 2E_{s0}\Delta e_s - V_{s0}\Delta e_s \cos\theta_{e0}{}^p - E_{s0}\Delta v_s \cos\theta_{e0}{}^p \\ &- E_{s0}V_{s0}\Delta\theta_g \sin\theta_{e0}{}^p + E_{s0}V_{s0}\Delta\theta_e \sin\theta_{e0}{}^p \end{aligned} \tag{46}$$

Combining (45) and (46), the grid voltage angle $\Delta\theta_g$ can be replaced by the following expression.

$$\begin{aligned} \Delta\theta_g = \Delta\theta_e &+ \frac{2\Delta e_s \sin\theta_{e0}^p}{E_{s0}} \\ &+ \frac{X_s\Delta P_s \cos\theta_{e0}^p - X_s\Delta Q_s \sin\theta_{e0}^p}{E_{s0}V_{s0}} \end{aligned} \tag{47}$$

The simplification of (47) can be achieved by assuming that $\sin\theta_{e0}^p \approx -1$ and $\cos\theta_{e0}^p \approx 0$.

$$\Delta\theta_g = \Delta\theta_e - \frac{2\Delta e_s}{E_{s0}} + \frac{X_s\Delta Q_s}{E_{s0}V_{s0}} \tag{48}$$

Therefore, $\Delta\theta_g$ is a function of $\Delta\theta_e$, Δe_s and ΔQ_s.

By applying (48), the DFIM internal voltage phase-amplitude dynamics can be updated as shown in Figure 11. Then, the internal voltage amplitude Δe_s is to be removed from (48). Since the reactive power through BTBPC is kept at 0, the stator reactive power Q_s is almost equal to the total input reactive power Q_t. Therefore, the transfer function from

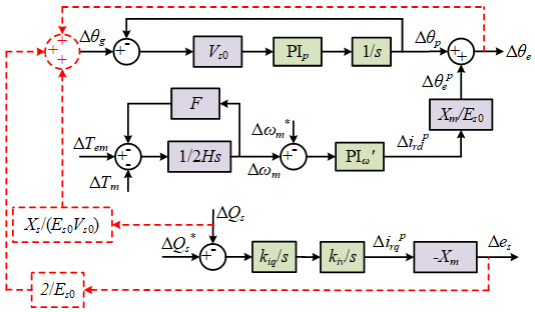

FIGURE 11. Updated DFIM internal voltage phase-amplitude dynamics.

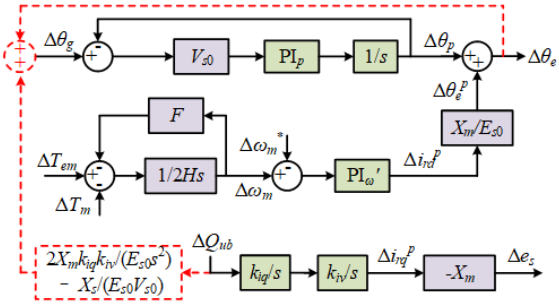

FIGURE 12. Further updated DFIM internal voltage phase-amplitude dynamics.

the unbalanced reactive power ΔQ_{ub} to the internal voltage amplitude Δe_s is expressed as

$$\Delta e_s = -X_m k_{iq} k_{iv} \Delta Q_{ub}/s^2 \tag{49}$$

where

$$\Delta Q_{ub} = \Delta Q_s^* - \Delta Q_s = -\Delta Q_s \tag{50}$$

Substitute (49) and (50) into (48),

$$\Delta\theta_g = \Delta\theta_e + (\frac{2X_m k_{iq} k_{iv}}{E_{s0}s^2} - \frac{X_s}{E_{s0}V_{s0}})\Delta Q_{ub} \tag{51}$$

Based on (51), the DFIM internal voltage phase-amplitude dynamics can be further updated, which is displayed in Figure 12. Furthermore, the transfer functions for $\Delta\theta_e$ and Δe_s are obtained by the deduction process in Figure 13.

$$\Delta\theta_e = (G_1 + G_1 G_4)\Delta T_{ub} + G_3 G_4 \Delta Q_{ub} \tag{52}$$

$$\Delta e_s = G_2 \Delta Q_{ub} \tag{53}$$

The expressions of $G_1 \sim G_4$ are shown in Appendix. G_1 is related to RSC; G_2 and G_3 are linked with RPC; G_4 is related to PLL. According to (52) and (53), it can be summarized that $\Delta\theta_e$ is determined by RSC, RPC and PLL, while Δe_s is dependent on RPC. Therefore, it is valuable to investigate the control effects of RSC, RPC and PLL on DFIM internal voltage phase-amplitude dynamics in the electromechanical control timescale.

V. SIMULATION RESULTS AND DISCUSSION

The simulation studies are carried out in Matlab/Simulink to verify the operation of a DFIM-SPS by applying the proposed interface friendly BTBPC average model, and the

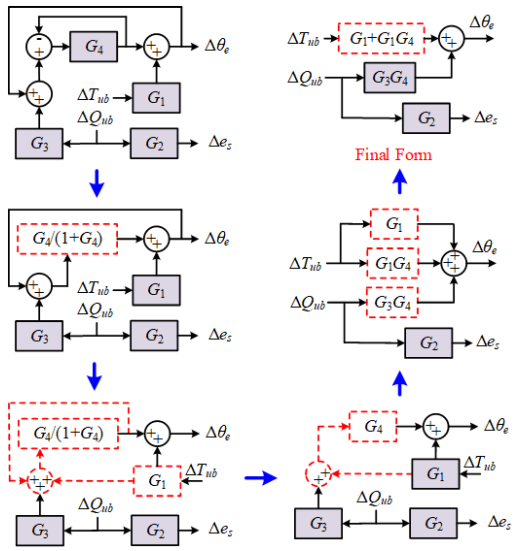

FIGURE 13. Further updated DFIM internal voltage phase-amplitude dynamics.

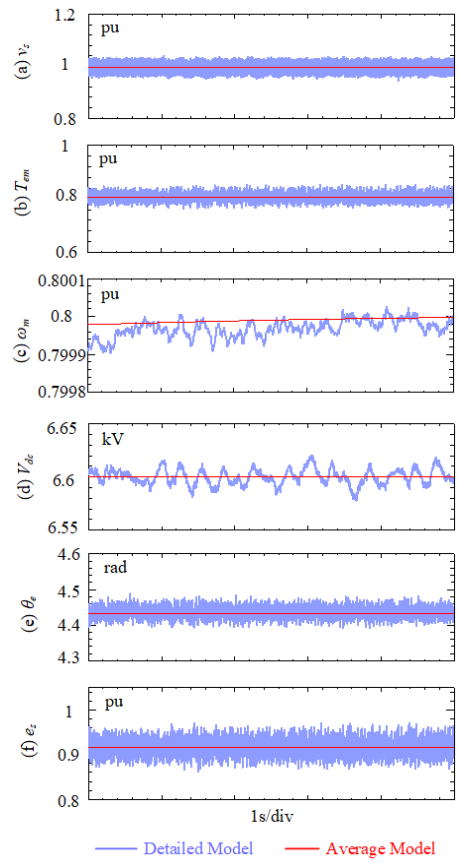

FIGURE 14. Comparison between the values of key variables derived by using the detailed and average BTBPC models (a) v_s (b) T_{em} (c) ω_m (d) V_{dc} (e) θ_e (f) e_s.

control effects of PLL, RSC and RPC on DFIM stator phase-amplitude dynamics are investigated. The time steps of 50μs and 100μs are applied for the DFIM-SPS discrete models with the detailed and average BTBPC models, respectively. The mechanical/load torque input for DFIM torque is 0.8pu,

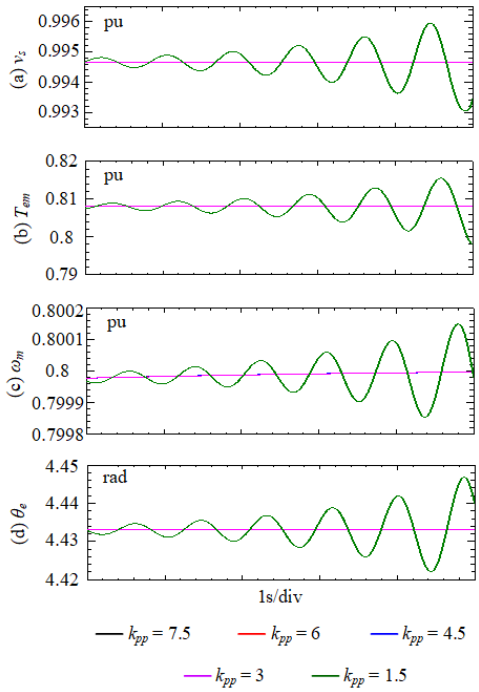

FIGURE 15. Control effects of varying k_{pp} on (a) v_s (b) T_{em} (c) ω_m (d) θ_e.

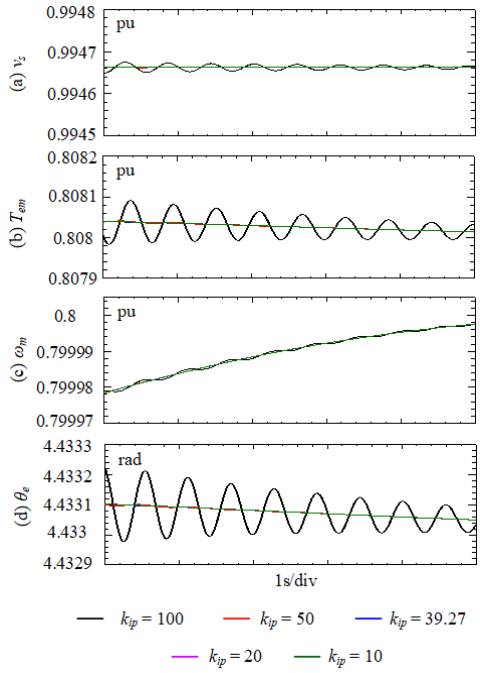

FIGURE 16. Control effects of varying k_{ip} on (a) v_s (b) T_{em} (c) ω_m (d) θ_e.

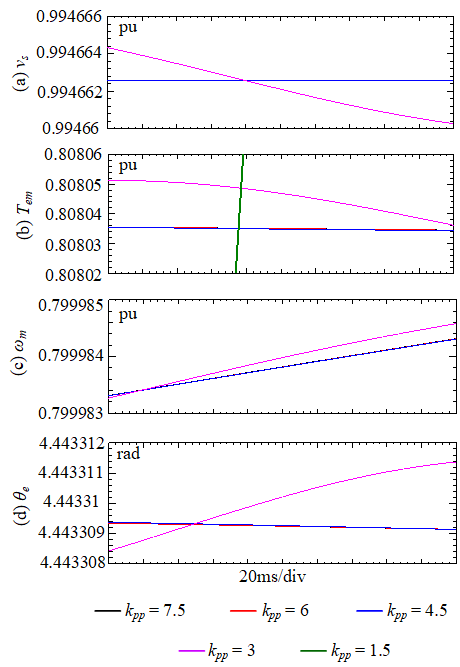

FIGURE 17. Enlarged drawing of Fig. 15 from 0.9s to 1.1s.

and the reference rotor speed is 0.8pu. The simulation parameters for the DFIM and SG, along with the primitive controller gains for RSC, RPC and PLL are displayed in Appendix.

The interface friendly BTBPC average model is applied in DFIM-SPS to reduce the time used for simulation, and the model is verified by comparing its performance to that of the detailed one. The key variables are compared for these two models, which are shown in Figure 14. It can be seen that oscillations are eliminated for the values derived by using the proposed average model of BTBPC, as the switching behaviors are omitted by replacing the switches with controlled voltage sources. The stator voltage v_s, electromagnetic torque T_{em}, rotor speed ω_m, and DC-bus voltage V_{dc} are all kept at nominal values when the ship operates at a specific operation point. The internal voltage phase θ_e is around $(-\pi/2)$, which is shown as a value close to $3\pi/2$ in the figure, and the internal voltage amplitude e_s is about 0.9pu, since the DFIM operates as a propulsion motor in the system.

In the electromechanical control timescale, the control effects of PLL, RSC and RPC are focused on. All of these control loops are related to the internal voltage phase dynamics, while only RPC affects the dynamics of internal voltage amplitude. The effects of varying PLL, RSC and RPC controller gains on system performance by applying the proposed interface friendly BTBPC average model are displayed in Figures 15–18, Figures 19 & 20, and Figures 21 & 22, respectively. When varying one of the controller gains, the others are kept at the primitive values, which are shown in Appendix.

It can be seen from Figure 15 that the PLL proportional gain k_{pp} is decreased from 7.5 to 1.5, with the step change of 1.5 to observe the effects on v_s, T_{em}, ω_m and the internal voltage phase θ_e. When the value of k_{pp} is large enough, the values of all these variables are kept stable. However, once k_{pp} is decreased to 1.5, the oscillation becomes more evident as the time goes, and eventually instable performance will be caused, which is not desirable. On the contrary, as can be seen from Figure 16, when the value of k_{ip} is small enough, the values of system variables track the corresponding values at the specific operation point very well. While obvious fluctuations

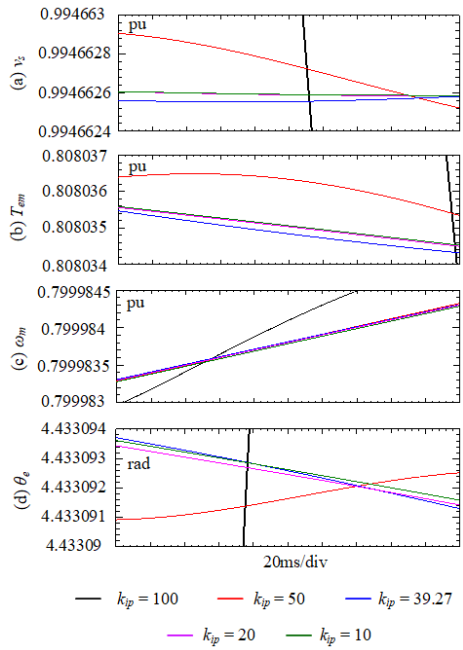

FIGURE 18. Enlarged drawing of Fig. 16 from 0.9s to 1.1s.

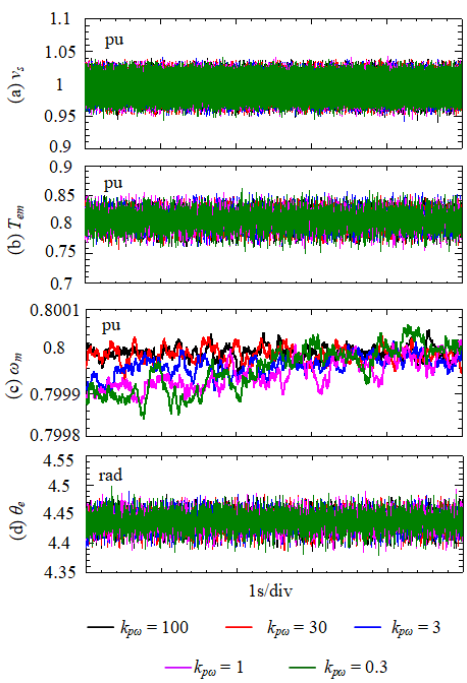

FIGURE 19. Control effects of varying k_{ip} on (a) v_s (b) T_{em} (c) ω_m (d) θ_e.

with decreasing amplitudes are presented when k_{ip} reaches 100, thus it takes much longer time for the system to achieve the stable operation.

In order to observe more details of applying different PLL controller gains on the system performance, the enlarged drawings of Figures 15 & 16 from 0.9s to 1.1s are displayed in Figures 17 & 18, respectively. Clear distinctions can only be seen by applying $k_{pp} = 3$ and $k_{ip} = 50$ when comparing

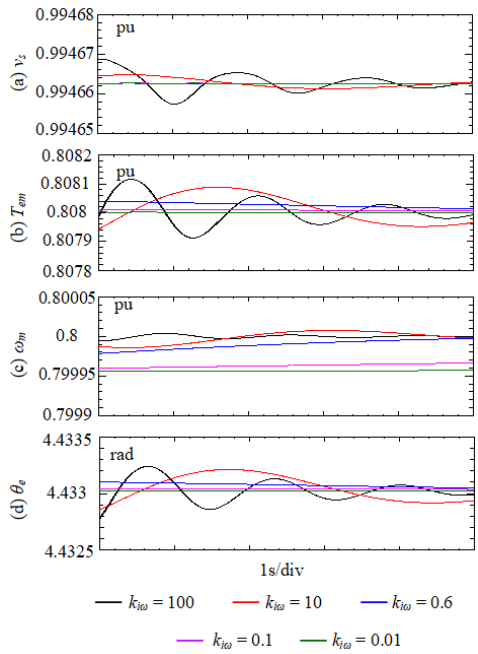

FIGURE 20. Control effects of varying $k_{i\omega}$ on (a) v_s (b) T_{em} (c) ω_m (d) θ_e.

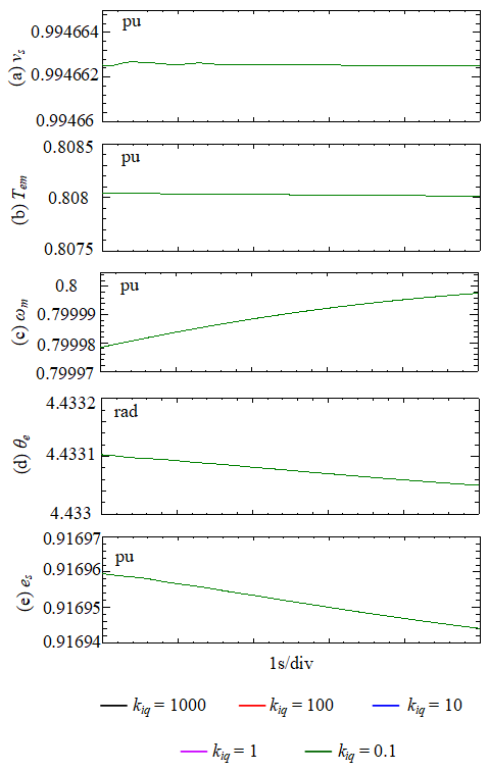

FIGURE 21. Control effects of varying $k_{i\omega}$ on (a) v_s (b) T_{em} (c) ω_m (d) θ_e.

to the plots with the other controller gain values (except $k_{pp} = 1.5$ and $k_{ip} = 100$) in Figures 17 & 18, respectively.

The control effects of varying RSC controller gains are presented in Figures 19 & 20. It can be seen that by changing the proportional gain $k_{p\omega}$, the values of these variables can track their reference values with some fluctuations, but good

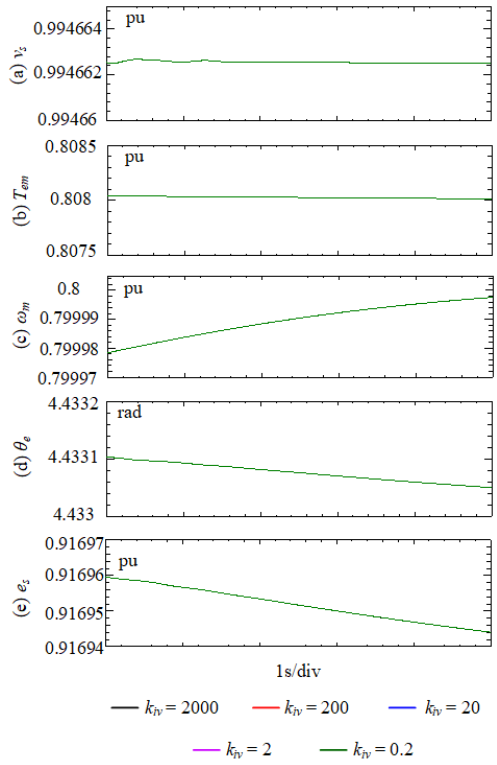

FIGURE 22. Control effects of varying k_{iv} on (a) v_s (b) T_{em} (c) ω_m (d) θ_e (e) e_s.

tracking performance is preserved. As the average BTBPC model is applied, the electromagnetic torque tracking accuracy is a little bit lower than using the detailed model, and the derived value of T_{em} is slightly higher than 0.8pu. From Figure 20, some distinctions in the system performance by using different integral gains are presented. Larger $k_{i\omega}$ results in more serious oscillations and longer time to achieve the steady operation point. However, as can be seen from Figure 20(c), the tracking accuracy is higher when the RSC integral gain becomes higher.

From (52) and (53), since the integral controller gains k_{iq} and k_{iv} always appear in the form of $k_{iq}k_{iv}$, the effect of varying the value of k_{iq} is the same as that of varying the value of k_{iv}. From Figures 21 & 22, the variations in k_{iq} and k_{iv} for RPC almost have no effects on the system performance, since the values of each variable when applying different values of k_{iq} and k_{iv} are equal to each other. This is because the calculation of stator reactive power Q_s is only dependent on the stator voltage and current, whose transient behaviors are eliminated due to the use of the proposed BTBPC average model, thus $\Delta Q_{ub} = 0$. According to (52) and (53), the effects of G_2 and G_3, which correspond to those of RPC, are therefore not reflected. Contrarily, as mentioned above, there are differences between the actual and reference electromechanical torque values, thus ΔT_{ub} is not 0, and the effects of G_1 (related to RSC) and G_4 (related to PLL) can be observed based on (52) when adjusting the values of k_{pp}, k_{ip}, $k_{p\omega}$ and $k_{i\omega}$.

VI. CONCLUSION

In this paper, a partially decoupled DFIM-SPS is proposed to enhance the system safety level by mitigating the dominating status of on-board power electronics. An interface friendly BTBPC average model is proposed for system-level analysis by replacing the switching behaviors with controlled voltage sources. Besides, a small-signal model for studying the DFIM internal voltage phase-amplitude dynamics in the electromechanical control timescale by considering the effects of BTBPC average model is proposed and illustrated. The control effects of RSC, RPC and PLL are taken into consideration for deriving the transfer functions of the internal voltage phase-amplitude dynamics in the concerned control timescale.

From the derived DFIM internal voltage phase and amplitude motion equations, and the simulation results obtained by applying the proposed BTBPC average model, the following key points are obtained.

1) The DFIM-SPS with the proposed interface friendly BTBPC average model can correctly simulate the system operation without considering the fast transients caused by switching behaviors.

2) The PLL proportional gain k_{pp} should be large enough to avoid instable operation, while the PLL integral gain k_{ip} needs to be small enough to ensure fast tracking performance.

3) A larger RSC integral gain $k_{i\omega}$ leads to more serious oscillations and longer time to achieve stable operation, but higher speed tracking performance is obtained.

4) The control effects of RPC cannot be explicitly investigated when the proposed BTBPC average model is presented, which is a drawback of the proposed model.

Detailed stability analysis will be performed in the authors' future work to provide clearer theoretical guidance on the controller design for the proposed DFIM-SPS.

APPENDIX

A. EXPRESSIONS OF TRANSFER FUNCTION BLOCKS

$$G_1 = \frac{X_m(k'_{p\omega}s + k'_{i\omega})}{E_{s0}(2Hs + F)s}, \tag{A.1}$$

$$G_2 = -\frac{X_m k_{iq} k_{i_v}}{s^2} \tag{A.2}$$

$$G_3 = \frac{2X_m k_{iq} k_{iv}}{E_{s0}s^2} - \frac{X_s}{E_{s0}V_{s0}}, \tag{A.3}$$

$$G_4 = V_{s0}\frac{k_{pps} + k_{ip}}{s^2} \tag{A.4}$$

B. DFIM PARAMETERS USED IN SIMULATION

P_{nom} = 4 MW/5MVA; V_{nom} = 4.16 kV; f_{nom} = 50 Hz; V_{dcnom} = 6.6 kV; C_{dc} = 30 mF; R_s = 0.023 pu; L_s = 3.08 pu; R_r = 0.016 pu; L_r = 3.06 pu; L_m = 2.9pu; $H = 3.5$ s; $F = 0.01$ pu; $n_p = 2$; $R_c = 0.003$ pu; $L_c = 0.3$pu.

C. SG PARAMETERS USED IN SIMULATION

P_{nom} = 4MW/5MVA; V_{nom} = 4.16kV; f_{nom} = 50Hz; n_p = 20; R_s = 0.036pu; X_d = 1.321pu; X'_d = 0.1685pu;

$X_d^{''} = 0.105$pu; $X_q = 1.173$pu; $X_q^{''} = 0.09$pu; $X_l = 0.075$pu; $T_{do}^{'} = 6.5$s; $T_{do}^{''} = 0.0241$s; $T_{qo}^{''} = 0.0464$s.

D. PRIMITIVE CONTROLLER GAINS

RSC: $k_{p\omega} = 3$, $k_{i\omega} = 0.6$; RPC: $k_{iq} = 20$, $k_{iv} = 10$; PLL: $k_{pp} = 4.5$, $k_{ip} = 39.27$.

REFERENCES

[1] Z. Jin, G. Sulligoi, R. Cuzner, L. Meng, J. C. Vasquez, and J. M. Guerrero, "Next-generation shipboard DC power system: Introduction smart grid and dc microgrid technologies into maritime electrical netowrks," *IEEE Electrific. Mag.*, vol. 4, no. 2, pp. 45–57, Jun. 2016.

[2] Z. Jin, L. Meng, J. M. Guerrero, and R. Han, "Hierarchical control design for a shipboard power system with DC distribution and energy storage aboard future more-electric ships," *IEEE Trans. Ind. Informat.*, vol. 14, no. 2, pp. 703–714, Feb. 2018.

[3] *IEEE Recommended Practice for 1 to 35 kV Medium Voltage DC Power Systems on Ships*, IEEE Standard 1709, 2010.

[4] F. Milano, F. Dörfler, G. Hug, D. J. Hill, and G. Verbič, "Foundations and challenges of low-inertia systems," presented at the Power Syst. Comput. Conf. (PSCC), Dublin, Ireland, 2018.

[5] J. Fang, H. Li, Y. Tang, and F. Blaabjerg, "On the inertia of future more-electronics power systems," *IEEE J. Emerg. Sel. Topics Power Electron.*, to be published.

[6] S. Yang, D. Xiang, A. Bryant, P. Mawby, L. Ran, and P. Tavner, "Condition monitoring for device reliability in power electronic converters: A review," *IEEE Trans. Power Electron.*, vol. 25, no. 11, pp. 2734–2752, Nov. 2010.

[7] P. Cairoli and R. A. Dougal, "Fault detection and isolation in medium-voltage DC microgrids: Coordination between supply power converters and bus contactors," *IEEE Trans. Power Electron.*, vol. 33, no. 5, pp. 4535–4546, May 2018.

[8] K. Satpathi, A. Ukil, and J. Pou, "Short-circuit fault management in DC electric ship propulsion system: Protection requirements, review of existing technologies and future research trends," *IEEE Trans. Transport. Electrific.*, vol. 4, no. 1, pp. 272–291, Mar. 2018.

[9] L. Qi, J. Pan, J. Daniel, O. Apeldoorn, J. Li, and Z. Wang, "Integrated converter modeling for medium voltage DC shipboard distribution system simulation," presented at the IEEE PES Gen. Meeting, National Harbor, MD, USA, Jul. 2014.

[10] L. Zhou, H. Liu, and L. Bai, "Modeling and simulation of all-electric ships with medium-voltage DC integrated power system," presented at the IEEE Conf. Expo Transp. Electrific. Asia–Pacific (ITEC Asia-Pacific), Beijing, China, 2014.

[11] S. Liu, W. Zhu, Y. Cheng, and B. Xing, "Modeling and small-signal stability analysis of an islanded DC microgrid with dynamic loads," presented at the IEEE 15th Int. Conf. Environ. Elect. Eng. (EEEIC), Rome, Italy, 2015.

[12] S. Chiniforoosh, J. Jatskevich, A. Yazdani, V. Sood, V. Dinavahi, J. A. Martinez, and A. Ramirez, "Definitions and applications of dynamic average models for analysis of power systems," *IEEE Trans. Power Del.*, vol. 25, no. 4, pp. 2655–2669, Oct. 2010.

[13] X. Wang, F. Blaabjerg, and W. Wu, "Modeling and analysis of harmonic stability in an AC power-electronics-based power system," *IEEE Trans. Power Electron.*, vol. 29, no. 12, pp. 6421–6432, Dec. 2014.

[14] B. Wen, D. Dong, D. Boroyevich, P. Mattavelli, R. Burgos, and Z. Shen, "Impedance-based analysis of grid-synchronization stability for three-phase paralleled converters," *IEEE Trans. Power Electron.*, vol. 31, no. 1, pp. 26–38, Jan. 2016.

[15] F. Yahyaie and P. W. Lehn, "On dynamic evaluation of harmonics using generalized averaging techniques," *IEEE Trans. Power Syst.*, vol. 30, no. 5, pp. 2216–2224, Sep. 2015.

[16] X. Liu, A. M. Cramer, and F. Pan, "Generalized average method for time-invariant modeling of inverters," *IEEE Trans. Circuits Syst. I, Reg. Papers*, vol. 64, no. 3, pp. 740–751, Mar. 2017.

[17] J. J. Rico, E. Acha, and T. J. E. Miller, "Harmonic domain modelling of three phase thyristor-controlled reactors by means of switching vectors and discrete convolutions," *IEEE Trans. Power Del.*, vol. 11, no. 3, pp. 1678–1684, Jul. 1996.

[18] J. J. Rico, M. Madrigal, and E. Acha, "Dynamic harmonic evolution using the extended harmonic domain," *IEEE Trans. Power Del.*, vol. 18, no. 2, pp. 587–594, Apr. 2003.

[19] J. R. C. Orillaza and A. R. Wood, "Harmonic state-space model of a controlled TCR," *IEEE Trans. Power Del.*, vol. 28, no. 1, pp. 197–205, Jan. 2013.

[20] J. Kwon, X. Wang, F. Blaabjerg, C. L. Bak, A. R. Wood, and N. R. Watson, "Linearized modeling methods of AC–DC converters for an accurate frequency response," *IEEE J. Emerg. Sel. Topics Power Electron.*, vol. 5, no. 4, pp. 1526–1541, Dec. 2017.

[21] B. Zahedi and L. E. Norum, "Modeling and simulation of all-electric ships with low-voltage DC hybrid power systems," *IEEE Trans. Power Electron.*, vol. 28, no. 10, pp. 4525–4537, Oct. 2013.

[22] J. Shi, R. Amgai, and S. Abdelwahed, "Modelling of shipboard medium-voltage direct current system for system level dynamic analysis," *IET Elect. Syst. Transp.*, vol. 5, no. 4, pp. 156–165, 2015.

[23] U. Javaid, F. D. Freijedo, D. Dujic, and W. van der Merwe, "Dynamic assessment of source–load interactions in marine MVDC distribution," *IEEE Trans. Ind. Electron.*, vol. 64, no. 6, pp. 4372–4381, Jun. 2017.

[24] X. Sun, L. Chen, Z. Yang, and H. Zhu, "Speed-sensorless vector control of a bearingless induction motor with artificial neural network inverse speed observer," *IEEE/ASME Trans. Mechatronics*, vol. 18, no. 4, pp. 1357–1366, Aug. 2013.

[25] X. Sun, L. Chen, H. Jiang, Z. Yang, J. Chen, and W. Zhang, "High-performance control for a bearingless permanent-magnet synchronous motor using neural network inverse scheme plus internal model controllers," *IEEE Trans. Ind. Electron.*, vol. 63, no. 6, pp. 3479–3488, Jun. 2016.

[26] X. Sun, Z. Shi, L. Chen, and Z. Yang, "Internal model control for a bearingless permanent magnet synchronous motor based on inverse system method," *IEEE Trans. Energy Convers.*, vol. 31, no. 4, pp. 1539–1548, Dec. 2016.

[27] H. Alafnan, M. Zhang, W. Yuan, J. Zhu, J. Li, M. Elshiekh, and X. Li, "Stability improvement of DC power systems in an all-electric ship using hybrid SMES/battery," *IEEE Trans. Appl. Supercond.*, vol. 28, no. 3, Apr. 2018, Art. no. 5700306.

[28] Y. Ji, Z. Yuan, J. Zhao, C. Lu, Y. Wang, Y. Zhao, Y. Li, and Y. Han, "Hierarchical control strategy for MVDC distribution network under large disturbance," *IET Gener., Transmiss. Distrib.*, vol. 12, no. 11, pp. 2557–2565, Jun. 2018.

[29] K. Satpathi, A. Ukil, S. S. Nag, J. Pou, and M. A. Zagrodnik, "DC marine power system: Transient behavior and fault management aspects," *IEEE Trans. Ind. Informat.*, vol. 15, no. 4, pp. 1911–1925, Apr. 2019.

[30] V. Nougain, S. Mishra, and A. K. Pradhan, "MVDC microgrid protection using a centralized communication with a localized backup scheme of adaptive parameters," *IEEE Trans. Power Del.*, vol. 34, no. 3, pp. 869–878, Feb. 2019.

[31] X. Sun, C. Hu, J. Zhu, S. Wang, W. Zhou, Z. Yang, G. Lei, K. Li, B. Zhu, and Y. Guo, "MPTC for PMSMs of EVs with multi-motor driven system considering optimal energy allocation," *IEEE Trans. Magn.*, vol. 55, no. 7, Jul. 2019, Art. no. 8104306.

[32] J. L. Kirtley, A. Banerjee, and S. Englebretson, "Motors for ship propulsion," *Proc. IEEE*, vol. 103, no. 12, pp. 2320–2332, Dec. 2015. doi: 10.1109/jproc.2015.2487044.

[33] J. Hu, L. Sun, X. Yuan, S. Wang, and Y. Chi, "Modeling of type 3 wind turbines with df/dt inertia control for system frequency response study," *IEEE Trans. Power Syst.*, vol. 32, no. 4, pp. 2799–2809, Jul. 2017.

[34] J. Hu, H. Yuan, and X. Yuan, "Modeling of DFIG-based WTs for small-signal stability analysis in DVC timescale in power electronized power systems," *IEEE Trans. Energy Convers.*, vol. 32, no. 3, pp. 1151–1165, Sep. 2017.

[35] J. Hu, Y. Huang, D. Wang, H. Yuan, and X. Yuan, "Modeling of grid-connected DFIG-based wind turbines for DC-link voltage stability analysis," *IEEE Trans. Sustain. Energy*, vol. 6, no. 4, pp. 1325–1336, Oct. 2015.

[36] M. Zhao, X. Yuan, and J. Hu, "Modeling of DFIG wind turbine based on internal voltage motion equation in power systems phase-amplitude dynamics analysis," *IEEE Trans. Power Syst.*, vol. 33, no. 2, pp. 1484–1495, Mar. 2018.

[37] W. Tang, J. Hu, Y. Chang, X. Yuan, and F. Liu, "Modeling of DFIG-based wind turbine for power system transient response analysis in rotor speed control timescale," *IEEE Trans. Power Syst.*, vol. 33, no. 6, pp. 6795–6805, Nov. 2018.

[38] A. K. Ådnanes, "Maritime electrical installations and diesel electric propulsion," ABB, Zürich, Switzerland, Tech. Rep. 2003-04-22, 2003.

[39] *IEEE Recommended Practice for Excitation System Models for Power System Stability Studies*, IEEE Standard P421.5, 1992.

KAI NI (S'17) was born in Suzhou, Jiangsu, China. He received the B.Eng. degree (Hons.) in electrical engineering and automation from Xi'an Jiaotong-Liverpool University, Suzhou, and the B.Eng. degree (Hons.) in electrical engineering from the University of Liverpool, Liverpool, U.K., in 2016, where he is currently pursuing the Ph.D. degree. His research interests include operation and control of doubly fed induction machines, power electronic converters, and power systems.

YIHUA HU (M'13–SM'15) received the B.S. degree in electrical engineering and the Ph.D. degree in power electronics and drives from the China University of Mining and Technology, in 2003 and 2011, respectively. From 2011 to 2013, he was with the College of Electrical Engineering, Zhejiang University, as a Postdoctoral Fellow. From 2013 to 2015, he was a Research Associate with the Power Electronics and Motor Drive Group, University of Strathclyde. He is currently a Lecturer with the Department of Electrical Engineering and Electronics, University of Liverpool (UoL). He has published 85 papers in IEEE Transactions journals. His research interests include renewable generation, power electronics converters and control, electric vehicle, more electric ship/aircraft, smart energy system, and non-destructive test technology. He is an Associate Editor of the IEEE Transactions on Industrial Electronics, *IET Renewable Power Generation*, *IET Intelligent Transport Systems*, and *Power Electronics and Drives*.

RUI LIANG received the B.Sc. and Ph.D. degrees from the Department of Electrical Engineering, China University of Mining and Technology (CUMT), in 2001 and 2010, respectively. Since 2001, he has been with the CUMT, he is currently a Professor with the Electrical Department, the Academic Committee Member of CUMT, the Executive Member of the Jiangsu Electrical Engineering Association, China, and the Deputy Director of the Jiangsu Province Laboratory of Electric and Automation. He has been awarded 15 patents and published two books and over 50 conference and journal publications. His current research interests include the protection in power grid, critical electrical equipment assessment, and modeling in energy interconnection.

HUIQING WEN (M'13–SM'18) received the B.S. and M.S. degrees in electrical engineering from Zhejiang University, Hangzhou, China, in 2002 and 2006, respectively, and the Ph.D. degree in electrical engineering from the Chinese Academy of Sciences, Beijing, China, in 2009. From 2009 to 2010, he was an Electrical Engineer with the GE (China) Research and Development Center Company, Ltd., Shanghai, China. From 2010 to 2011, he was an Engineer with the China Coal Research Institute, Beijing. From 2011 to 2012, he was a Postdoctoral Fellow with the Masdar Institute of Science and Technology, Abu Dhabi, United Arab Emirates. In 2013, he joined the Electrical and Electronic Engineering Department, Xi'an Jiaotong-Liverpool University (XJTLU), Suzhou, China, where he is currently a Senior Associate Professor. He has published more than 100 peer-reviewed technical papers in leading journals/conferences and holds over 20 issued/pending patents. His research interests include renewable energy, electric vehicle, power electronics, microgrid, and power semiconductor devices. He is an Associate Editor of the IEEE Access, *International Journal of Photoenergy*, and *Journal of Power Electronics*.

MOHAMMED ALKAHTANI was born in Ar Rayn, Saudi Arabia. He received the B.Eng. degree (Hons.) in electrical and electronics engineering and the M.Sc. degree in electrical power and control engineering from Liverpool John Moores University, Liverpool, U.K., in 2014 and 2016, respectively. He is currently pursuing the Ph.D. degree with the University of Liverpool. His research interests include soiling management of photovoltaic and a PV array efficiency improvement.